ADVANCED ENGINEERING MATERIALS
www.aem-journal.com

An Integrated MATLAB Code for Homogenization-Based Topology Optimization and Generating Functionally Graded Surface Lattices for Additive Manufacturing

Mirhan Ozdemir, Ugur Simsek, Cemal Efe Gayir, Kadir Gunaydin, and Orhan Gulcan*

Triply periodic minimal surfaces (TPMS) lattices are gaining popularity for enhancing structural efficiency in many engineering applications. Functionally graded TPMS structures provide more customized mechanical properties and improved functionality compared to typical homogenous designs by deliberately altering material properties throughout the lattice. This study presents a novel framework by integrating a homogenization-based topology optimization method with functionally graded lattice creation, utilizing a streamlined and versatile MATLAB code. The methodology encompasses several essential phases, including preprocessing, finite element analysis, sensitivity analysis, density filtering, optimization, element density visualization, and lattice reconstruction. These steps facilitate the development of highly efficient lattice structures with varied attributes, rendering them optimal for additive manufacturing and full-scale analysis. To ensure the accuracy of the established methodology, three optimization case studies with different boundary conditions are defined, and the mechanical reactions of the optimized lattice structures in filled with different TPMS structures are extensively validated by comparing them to both full-scale finite element models and experiments. The comparative results demonstrate that the mechanical responses obtained from topological analysis closely correspond to those acquired from full-scale models and experiments.

1. Introduction

Lattice structures are complex 3D formations composed of interconnected struts and walls that form repeating unit cells.[1,2] Triply periodic minimal surfaces (TPMS) structures are a fascinating member of the lattice family that can be generated using mathematical formulas and offer the advantage of being able to alter their mechanical performance by adjusting the design parameters.[3] These forms of TPMS structures are referred to as functionally graded lattice (FGL) structures that exhibit gradual changes in volume density, type, or unit-cell size throughout the material's volume. The variation in FGL structures throughout their volumes enables the modification of physical properties such as mass density, specific heat, thermal conductivity, corrosion and wear resistance, and hardness, depending on the needs of relevant applications.[4–6]

Understanding the mechanical properties of lattice structures is crucial for their effective application in a wide range of industrial contexts. Performing mechanical tests allows for the quantification of the mechanical properties of lattice structures. Nevertheless, these tests can be quite expensive and require a significant amount of time. Thus, numerical analyses can be conducted to precisely determine the necessary material properties. Lattice structures consist of periodic unit cells (PUC) that simplify numerical models and expedite the evaluation process through the utilization of

M. Ozdemir, U. Simsek
Department of Mechanical Engineering
Ozyegin University
34794 Istanbul, Türkiye
E-mail: ugur.simsek.16339@ozu.edu.tr

M. Ozdemir
Institute of Nanotechnology
Karlsruhe Institute of Technology
76344 Eggenstein-Leopoldshafen, Germany

The ORCID identification number(s) for the author(s) of this article can be found under https://doi.org/10.1002/adem.202402567.

DOI: 10.1002/adem.202402567

U. Simsek
Department of Mechanical Engineering
University of Michigan
48109 Ann Arbor, MI, USA

C. E. Gayir
Department of Mechanical Engineering
Koc University
34450 Istanbul, Türkiye

K. Gunaydin, O. Gulcan
General Electric Aerospace
Türkiye Technology Center
34880 İstanbul, Türkiye

a model reduction technique called homogenization.[7–9] By utilizing homogenization theory, this approach determines the material properties of lattice structures by analyzing the effective macro-scale behavior of PUC.[10] This PUC demonstrates similar characteristics (such as stress, strain, displacement, etc.) as the macrolattice structure. Thus, the quantitative calculation of the lattice structures' macroscopic behavior can be achieved by analyzing the behavior of PUC. The scientific literature explores various methods for homogenization, including asymptotic homogenization, machine learning, multiscale homogenization, solid-state physics, micropolar theory, surface or volume averaging, and beam theory.[11–17]

To enhance component performance within design limitations, topology optimization (TO) methods have been extensively employed in various industrial applications, including automotive,[18] healthcare,[19] aerospace,[20] and architecture.[21] There is a wide range of TO approaches that have been extensively studied and documented in the literature.[22–25] In addition, the aforementioned homogenization methods can be directly integrated into TO in order to achieve FGL geometries that fulfill specific requirements for applications.[26,27] According to Plocher and Panesar, the utilization of lattice structures as infill geometries and TO serves as the foundation for the development of advanced lightweight structures.[28] Li et al. utilized the asymptotic homogenization method to analyze a unit-cell and determine the equivalent elastic material properties corresponding to various relative densities. They then incorporated these properties into TO in order to calculate the most effective distribution of element density. The study showed that FGL structures demonstrated greater stiffness and improved heat conductivity in comparison to uniform lattice structures.[29] In order to achieve the best element densities, Cheng et al. utilized a nongradient-based proportional TO approach. This study focused on characterizing the effective material properties of the unit cells using the elastic scale law. To validate the proposed method, full-scale simulations and experiments were conducted. They demonstrated that the optimized geometry closely matched the experimental results.[30] In a separate study, Simsek et al. put forward a revised solid isotropic material with penalisation (SIMP) method. They made adjustments to the material constant and exponent of the SIMP formula based on curves derived from homogenization analysis involving various relative densities. The effectiveness of the suggested design was proven through the use of a structure filled with double gyroid lattice structures.[31] Ozdemir et al. successfully created FGL structures of various shapes (Diamond, Gyroid, I-WP, and Primitive) using genetic algorithms and anisotropic homogenization-based TO. A genetic algorithm was utilized to find the most efficient lattice structure, which was then evaluated using homogenization-based TO. The results indicate that the proposed method yields FGL structures with higher stiffness compared to single lattice morphologies.[32] In a recent study, an open-source GPU solver for large-scale inverse homogenization problems was introduced by Zhang et al.[33] This code enables the application of periodic boundary conditions and utilizes the parallel computation power of a memory-efficient GPU solver. The homogenized stiffness terms, such as bulk modulus, shear modulus, and Poisson's ratio, can be optimized under a predefined set of constraints using this code, and optimized microstructures with respect to desired material properties are reported in a library. This study is confined to identifying optimum microstructures and does not address the infilling of an extensive design domain comprising numerous functionally graded microstructures for fully exploiting the capabilities of lattice structures. One key aspect, the implicit formulation of optimized microstructures required for the generation of FGL structures, is reported as part of future work.

Although previous studies have explored homogenization, TO with public codes for various TO problems,[34–58] and TPMS modeling separately, the entire scheme has not been discussed in a versatile coding framework that includes homogenization of TPMS structures, integration of homogenization material properties into TO, generation of FGL structures from TO results, and exporting data for additive manufacturing (AM) and full-scale finite element analysis (FEA) for validation. In order to address this issue, a streamlined MATLAB code has been developed in this study. For this purpose, the material model, element stiffness matrices, and sensitivity calculations have been modified in the existing SIMP-based 3D TO scheme[40] to perform anisotropic homogenization-based TO. Another key contribution is to map element densities attained from TO onto given TPMS unit-cells to create graded lattice structures. In the author's previous studies, relative density mapping (RDM),[32,59] radial basis function (RBF) mapping,[31] and sensitivity-based mapping scheme[60] have been implemented and compared for graded lattice generation. Besides, in a more recent study, a gradient method was introduced by Modrek et al.,[61] in which the relative densities of a set of elements in the xz-plane at a specific y-value are averaged to generate graded cellular structures along the y-axis. In a heat sink thermal conductivity problem, the mapping effectiveness of the structures obtained by RDM and gradient methods was compared with the unmapped optimization results, confirming the superiority of the proposed gradient mapping method. In addition to producing graded structures by altering relative densities with a fixed unit-cell size, a correlation between the period and cell size can be established by varying the unit-cell size while maintaining constant relative densities across the domain. This enables the efficient reduction of mean curvature deviations and geometric distortions, while permitting localized control of TPMS.[62] However, based on the author's prior expertise and the clarity and intuitiveness of the suggested code architecture, the reconstruction module has been newly developed to produce a fixed unit-cell size by varying relative densities using the RDM approach. The reconstruction module generates stereolithography (STL) models for AM and voxel mesh models for full-scale FE validation analyses. To validate the proposed code, three case studies have been established, each with distinct boundary conditions, and full-scale voxel models have been constructed utilizing the data obtained from TO to numerically corroborate TO results. Finally, for experimental validation, the optimized geometries attained from three case studies have been printed using the material jetting AM method and subjected to mechanical testing. The comparative findings confirm the superior properties of FGL structures over uniform structures, as well as the accuracy of the generated code.

The remainder of this study is organized as follows. In Section 2, we introduce the methodologies used for lattice

generation and anisotropic homogenization. In Section 3, the details of coding implementation are discussed. Section 4 is dedicated to numerical examples. It provides a concise explanation of the compliance minimization TO problem formulation with volume constraints, modifications in the existing TO codes, and novel FGL generation codes. Section 5 is reserved for AM of the optimized FGL structures and experimental validations, and finally, our main conclusions are outlined in Section 6.

2. Materials and Methods

2.1. Surface-Based Lattice Design

This section will explore the formulation and design of surface-based lattices and their potential for creating various lattice types. TPMS structures can be modeled by employing an implicit mathematical equation $U(x, y, z, t) = 0$.[63,64] Here, x, y, and z denote coordinates on the iso-surface, while t, referred to as "level set parameters," indicates the necessary offset for generating a volume from the iso-surface. The value of t is crucial in lattice design as it directly affects the relative density ρ^*. The relative density represents the density ratio of porous $\rho_{\text{latt.}}$ to solid $\rho_{\text{sol.}}$ ($\rho^* = \rho_{\text{latt.}}/\rho_{\text{sol.}}$). This study analyzes and formulates six lattice types, namely Diamond (D), Fischer–Koch (FK), F-RD, Gyroid (G), I-WP, and Primitive (P). which are depicted in **Table 1**.

The unique connection between t and ρ^* must be determined separately for each lattice. One method involves systematically adjusting the t value and measuring the resulting lattice density. Hence, ρ^* can be computed using t and its corresponding ρ^* value through mathematical equations. The relative density ranges from 0 to 1, representing fully porous ($\rho^* = 0$) and solid ($\rho^* = 1$) states. As t increases, ρ^* approaches unity, indicating less porosity. To account for the lattice's structure with voids, it is practical to focus on specific ρ^* ranges, constraining the possible t values. The relationship between t and ρ^* for six different lattices is depicted in **Figure 1**.

Once the distinct relationship between t and ρ^* is established for each lattice individually, the mechanical properties of the lattice can be determined based on its geometric features using various modeling methods. The upcoming section will discuss the anisotropic homogenization of the lattices, which connects their elastic stiffness constants with ρ^*.

2.2. Anisotropic Homogenization of Lattice Morphology

Due to the cubic symmetry[65] of the TPMS lattices, the stiffness matrix's relationship can be simplified as follows: $C_{11} = C_{22} = C_{33}$, $C_{12} = C_{13} = C_{23}$, and $C_{44} = C_{55} = C_{66}$, while the remaining elements are zero. With this simplification, the mechanical

Table 1. Mathematical equation and geometry of the TPMS lattices.[63,64]

Equation	Geometry ($\rho^* = 0.2$)
$f_D = [\sin(k_x x) \times \sin(k_y y) \times \sin(k_z z) + \sin(k_x x) \times \cos(k_y y) \times \cos(k_z z) + \cos(k_x x) \times \sin(k_y y) \times \cos(k_z z) + \cos(k_x x) \times \cos(k_y y) \times \sin(k_z z)]^2 - t^2$	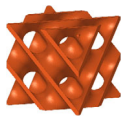
$f_{FK} = [\cos(2k_x x) \times \sin(k_y y) \times \cos(k_z z) + \cos(2k_y y) \times \sin(k_z z) \times \cos(k_x x) + \cos(2k_z z) \times \sin(k_x x) \times \cos(k_y y)]^2 - t^2$	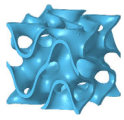
$f_{F-RD} = [-4 \times \cos(k_x x) \times \cos(k_y y) \times \cos(k_z z) - \cos(2k_x x) \times \cos(2k_y y) - \cos(2k_y y) \times \cos(2_z z) - \cos(2k_x x) \times \cos(2k_z z)]^2 - t^2$	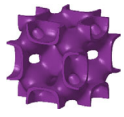
$f_G = [\cos(k_x x) \times \sin(k_y y) + \cos(k_y y) \times \sin(k_z z) + \sin(k_x x) \times \cos(k_z z)]^2 - t^2$	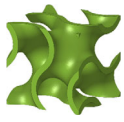
$f_{I-WP} = [2 \times (\cos(k_x x) \times \cos(k_y y) + \cos(k_y y) \times \cos(k_z z) + \cos(k_x x) \times \cos(k_z z)) - (\cos(2k_x x) + \cos(2k_y y) + \cos(2k_z z))]^2 - t^2$	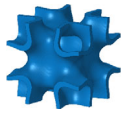
$f_P = [\cos(k_x x) + \cos(k_y y) + \cos(k_z z)]^2 - t^2$	
where $k_i = (2\pi/l_i) \times i$ and $i = x$, y, and z.	

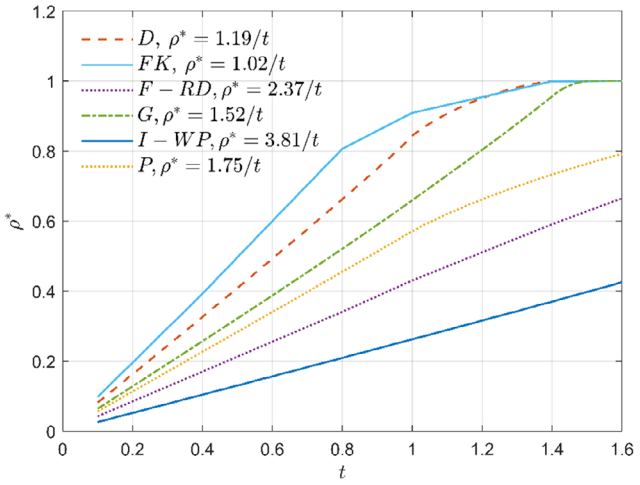

Figure 1. t to ρ^* mapping for different lattices.

properties of TPMS structures can be described using three distinct stiffness constants as follows

$$C_{\text{TPMS}} = \begin{bmatrix} C_{11} & C_{12} & C_{12} & 0 & 0 & 0 \\ C_{12} & C_{11} & C_{12} & 0 & 0 & 0 \\ C_{12} & C_{12} & C_{11} & 0 & 0 & 0 \\ 0 & 0 & 0 & C_{44} & 0 & 0 \\ 0 & 0 & 0 & 0 & C_{44} & 0 \\ 0 & 0 & 0 & 0 & 0 & C_{44} \end{bmatrix} \tag{1}$$

To determine these three stiffness constants, a single TPMS unit cell should be subjected to a normal and shear loading, separately. In each loading, one strain component is set to unity, while the others are set to zero during the numerical implementation as given in Equation (2).[66] This approach allows for a simplified characterization of the mechanical behavior of TPMS structures.

$$\text{Input:} \begin{Bmatrix} \varepsilon_{11} \\ \varepsilon_{22} \\ \varepsilon_{33} \\ \varepsilon_{23} \\ \varepsilon_{31} \\ \varepsilon_{12} \end{Bmatrix} = \begin{Bmatrix} 1 \\ 0 \\ 0 \\ 0 \\ 0 \\ 0 \end{Bmatrix} \quad \text{Output:} \begin{Bmatrix} \sigma_{11} \\ \sigma_{22} \\ \sigma_{33} \\ \sigma_{23} \\ \sigma_{31} \\ \sigma_{12} \end{Bmatrix} = \begin{Bmatrix} C_{11} \\ C_{21} \\ C_{31} \\ C_{41} \\ C_{51} \\ C_{61} \end{Bmatrix} \tag{2}$$

For practical applications, in the normal loading case to extract C_{11} and C_{12}, a strain of 1% of the structure's length is applied to the top face, while the other faces remain fixed along their normal. The boundary condition for the normal loading is expressed mathematically as given in Equation (3) and schematically illustrated in **Figure 2**a, where l_x, l_y, and l_z represent the total length of the structure in the x, y, and z directions, respectively.

$$\begin{aligned} &\Delta l_x|_{x=l_x} = 0.01 l_x \\ &\Delta l_x|_{x=0} = \Delta l_y|_{y=l_y} = \Delta l_y|_{y=0} = \Delta l_z|_{z=l_z} = \Delta l_z|_{z=0} = 0 \end{aligned} \tag{3}$$

For the shear loading case, a shear strain of 0.5% is applied to two surfaces, as boundary conditions are mathematically given in Equation (4) and illustrated schematically in Figure 2b.

$$\begin{aligned} &\Delta l_x|_{z=l_x} = 0.005 l_z,\ \Delta l_z|_{x=l_z} = 0.005 l_x \\ &\Delta l_z|_{x=0} = \Delta l_y|_{y=l_y} = \Delta l_y|_{y=0} = \Delta l_z|_{z=l_z} = \Delta l_x|_{z=0} = 0 \end{aligned} \tag{4}$$

To determine the values of C_{11} and C_{44}, reaction forces over nodes on the loaded surfaces are integrated. In the scenario of normal strain loading, the reaction force on one of the side surfaces is calculated to obtain the value of C_{12}, utilizing the formula provided below.

$$C_{11} = \frac{R_{11} \times A_{11}}{\varepsilon_{11}} \quad C_{12} = \frac{R_{12} \times A_{12}}{\varepsilon_{12}} \quad C_{44} = \frac{R_{44} \times A_{44}}{\varepsilon_{44}} \tag{5}$$

where R_{ij}, A_{ij}, and ϵ_{ij} are the total reaction force, area of interest, and total strain applied to the boundaries, respectively.

The analysis procedure is iterated for a specific relative density range of interest, varying between 0.1 and 0.5 with increments of

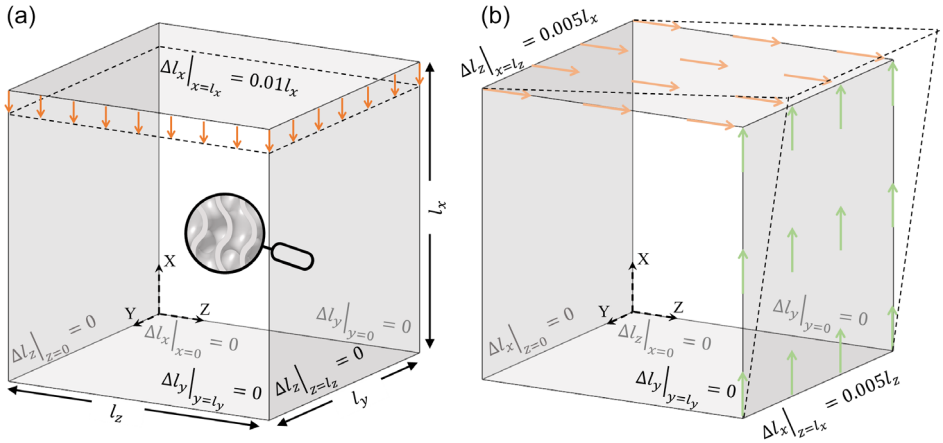

Figure 2. Normal and shear boundary conditions.

0.1 for this study. Stiffness values for each TPMS lattice are estimated as a function of relative density using a scale-law equation. The stiffness coefficients are represented using the second-order polynomial curves, $C_{ij} = p_1 \times (\rho^*)^2 + p_2 \times (\rho^*) + p_3$, along with corresponding R^2 values, which are detailed in **Table 2**. These trends are visually depicted in **Figure 3**a–c.

3. Implementation Details

Once the mechanical characterization of the TPMS lattices is studied to define the homogenization curves, the designer may integrate the defined curves into the developed optimization code to generate FGL. **Figure 4** illustrates the flow diagram of the proposed code. The process begins with the preprocessing phase, where essential constants for the polynomial curves obtained from homogenization analyses, along with design parameters for creating optimization geometry, are defined. Following the determination of parameters for a specific optimization case study, the TO process ensures an optimal material distribution while meeting specified constraints. Once TO reaches convergence, the material distribution is displayed for post-processing. Topology-optimized designs, being intricate, can pose challenges in reproducing them for subsequent FEA and manufacturing preparations. Hence, the subsequent step in the suggested flow involves reconstructing the optimized design. Designers have the flexibility to choose either STL or voxel format for reconstruction to facilitate further analysis or manufacturing requirements. For the purposes of this study, a MATLAB script implementing this methodology has been provided.

The proposed flowchart smoothly integrates existing MATLAB functions and subfunctions or utilizes open-source code to achieve the predefined objectives. These are also listed in **Table 3**, accompanied by brief descriptions.

3.1. Parameter Definition

The script commences by establishing multiple parameters, such as material properties, geometric design specifications, applied loads, TO parameters, and the concluding phase of reconstruction. At first, the material properties are assigned as `scale_law` and `base_material` to their respective domains, assessing the material's response under various conditions. The preceding chapter elucidates the implementation of homogenization in relation to the scale law and offers polynomial curve approximations for different lattice configurations. Designers possess the autonomy to select the lattice type and determine the size of its unit cell, thereafter, examining the homogenization curves that have been defined. The plates are coated with the base material, which contains isotropic properties, elastic modulus, and Poisson's ratio. Once the material parameters have been established, the subsequent stage entails specifying the geometric characteristics. The dimensions of the design domain are determined by the cubic unit-cell size (`cell_size`) and the number of unit cells in each direction (`cell_counts`). For example, if the cell size is 10 mm and the cell counts are [3 2 1] the resulting design domain would have dimensions of 30 mm in the *x*-direction, 20 mm in the *y*-direction, and 10 mm in the *z*-direction. Furthermore, the specification of `plate_thickness` is of utmost importance in sandwich designs, where the plates are oriented in the *x*–*z* plane. Load boundary constraints are defined according to the geometric specification. The `total_load` is uniformly distributed based on the needs of the case study. Afterward, the parameters for TO are established, which consist of minimum, maximum, and target volume fractions that act as constraints. It is important to note that plates are considered passive elements and are not subject to examination for convergence in TO. The additional parameters, namely `r_min` (minimum radius), `max_loop` (maximum iteration number), and `tol_x` (tolerance value for convergence), are specified. In addition, the `displayflag_loop` parameter allows for the visualization of material distribution at each iteration, which leads to a longer convergence time. Finally, the parameters for the reconstruction of optimum designs are defined. The `mesh_scaling` controls the level of mesh refinement in reconstructed geometries, thereby affecting the resulting file size. Designers have the option to choose voxel (.fem) or 2D surface mesh (.stl) reconstructions. The voxel reconstruction is used for FEA, while the surface mesh reconstruction is used for AM. **Table 4** presents a concise overview of these factors for convenient reference. The details and usage of the design variables are thoroughly explained in the following subsections.

3.2. Preprocessor

The scale-law constants and constitutive material properties, represented by `scale_law` and `base_material`, are defined. These parameters serve as the foundation for subsequent calculations within the script. With these values in

Table 2. Constants of second-order polynomials for six different TPMS structures.

TPMS	C_{11}				C_{12}				C_{44}			
	a_{11}	a_{12}	a_{13}	R^2	b_{11}	b_{12}	b_{13}	R^2	c_{11}	c_{12}	c_{13}	R^2
D	1556.3	738.0	37.1	0.999	840.0	302.8	21.6	0.998	604.6	118.8	4.5	1
G	1598.0	657.6	29.6	0.999	661.9	406.0	15.6	0.999	515.8	167.0	4.4	1
P	2758.2	156.4	54.4	0.999	1116	277.4	34.0	0.998	457.7	259.9	6.4	1
FK	1956	584.8	26.04	0.9996	866.8	279.7	19.89	0.9988	582.7	126.8	4.138	0.9999
I-WP	2496	434	4.745	0.9999	1259	11.22	14.67	0.9993	561.2	78.25	9.148	0.9996
F-RD	3194	287.9	46.51	0.9996	2064	−209.2	40.83	0.9986	695.9	101	0.6273	0.9998

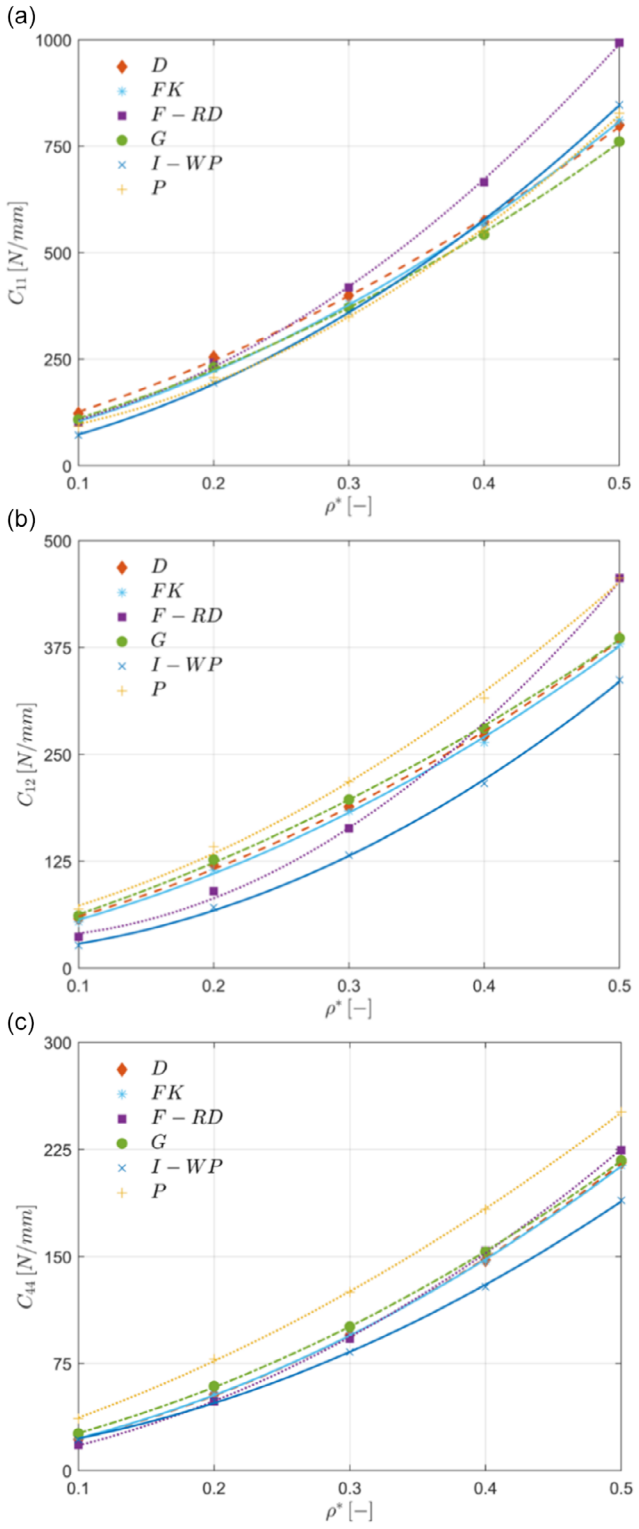

Figure 3. Stiffness terms a) C_{11}, b) C_{12}, and c) C_{44} for different lattice types using homogenization analyses.

place, the script proceeds to compute essential stiffness matrix variables, including C_{11}, C_{12}, and C_{44}, vital for further analysis and characterization of the material's behavior.

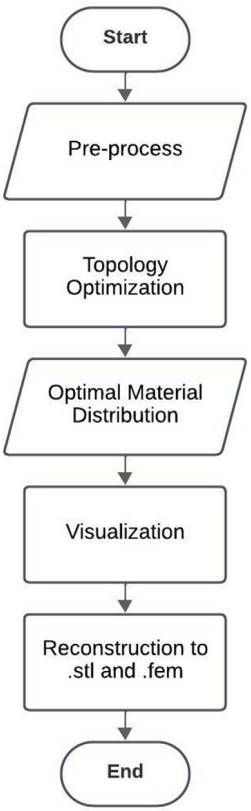

Figure 4. Flowchart of the proposed algorithm.

$$\begin{bmatrix} a_{11} & a_{12} & a_{13} \\ b_{11} & b_{12} & b_{13} \\ c_{11} & c_{12} & c_{13} \end{bmatrix} \tag{6}$$

Geometric parameters of the design domain are defined at the preprocessing stage prior to. The complete MATLAB script is available in the Supporting Information, and the preprocessing parameter can be defined or modified on script lines 2–26. After preprocess parameters, including material properties, geometric dimensions, and optimization parameters, are defined, the script becomes ready for conducting homogenization-based TO.

3.3. TO

A major improvement of the proposed approach is the replacement of the conventional SIMP material model with three polynomials calculated from homogenization analyses. Therefore, an efficient open source TO code using the SIMP method is utilized in this study.[40] The material model, element stiffness matrix[67] used in the finite element calculations, sensitivity calculations, and visualization sections are modified to perform homogenization-based TO. Therefore, more details about each step can be found in the referenced study. In the optimization step, the stiffness matrix is computed for each element within a given design domain using the novel material model, with the element density value being determined by the optimizer. This process is done iteratively until convergence, defined as the point where the

Table 3. Functions and their description.

Function	Line	Description
top3d.m	1–137	TO and FEA[40]
display_3D.m	144–169	Display TO density distribution[40]
hex.m	169–240	Compute stiffness matrix for brick element[67]
hex_sens.m	241–309	Compute sensitivity matrix for the brick element
element_setup.m	310–317	Recreating element connectivity array by excluding plates and assigning corresponding element densities for reconstruction
averaging_densities.m	318–334	Averaging element densities for reconstruction
reconstruct.m	335–394	Regeneration of topology optimized design

Table 4. Design variables and their description.

Design variables	Description
Material	
scale_law	Lattice scale law C_{11}, C_{12}, and C_{44} constants
base_material	Base material properties
Preprocess	
cell_size	Unit-cell size
cell_counts	Number of unit-cell in *x*, *y*, and *z* directions
plate_thickness	Plate thickness
total_load	Applied total load
Solution	
minumum_volfrac	Minimum volume fraction
maximum_volfrac	Maximum volume fraction
target_volfrac	Target volume fraction
r_min	Minimum radius
max_loop	Maximum number of loops
tol_x	Tolerance
displayflag_loop	Plotting material distribution at each loop switch 1, on; 0, off
Lattice Morphology	
f	Lattice iso-surface equation
ftf	Lattice t to ρ^* mapping
Reconstruction	
mesh_scaling	Mesh density for reconstructed geometry
fem_reconstruction	.fem reconstruction switch 1, on; 0, off
stl_reconstruction	.stl reconstruction switch 1, on; 0, off

objective value changes by an amount that is smaller than the predefined tolerance value. Furthermore, if the lattice structure is sandwiched between two plates, with a nonzero value for the plate_thickness parameter, isotropic material properties are assigned to elements of the plates. However, these elements remain passive during the optimization process. The implementation of stiffness terms for each element utilizing scale-law constants is detailed in code lines 170–186 of the MATLAB script (see Supporting Information).

In order to incorporate the new material model, modifications to the sensitivity matrix calculations are also necessary. Sensitivity analysis is essentially a method used to determine how changes in material density affect the objective function. The design variables are updated iteratively to satisfy optimization constraints, such as the desired volume fraction and minimum and maximum relative density thresholds. The script provides detailed output describing the progress of each iteration, including information about the goal function value and volume fraction. Furthermore, there is an option to include a 3D representation of the material density distribution. The code for calculating the sensitivity matrix is included in lines 106–117 of the MATLAB script (see Supporting Information).

3.4. Visualization

As a means to visualize the results, the script uses minimum and maximum element density thresholds and other user-defined parameters to generate a representation of the optimized design domain. The values of those parameters are defined as minimum and maximum relative densities by default, yet the designer is free to set a different range of values. Using MATLAB's patch function, the script iterates through each element in the design domain, utilizing their position and density to render them as 3D patches, with the color intensity being adjusted based on their relative density. This process helps the designer understand the results of their work and allows them to do more research and make improvements. **Figure 5** illustrates the material distribution of a topology-optimized beam with varying minimum and maximum element density thresholds.

Executing the given script creates a picture of the optimal material distribution for the structure, showing how the material density is spread out in space across the design domain. By grading black and gray colors to different density ranges, the visualization offers insights into the structural composition and optimization progress. Here, ideally, white is for lower densities, whereas higher densities are represented by gray colors (see Figure 5). Such visual representations not only enhance understanding but also serve as valuable tools for communicating design concepts and findings. Going forward, these visualizations can help with iterative optimization processes and looking into different configurations for more rebuilding and improvement steps.

3.5. Reconstruction

The mapping of element densities over a given design domain to construct optimized graded lattice structures has been extensively studied in the literature.[60,61] A widely adopted approach

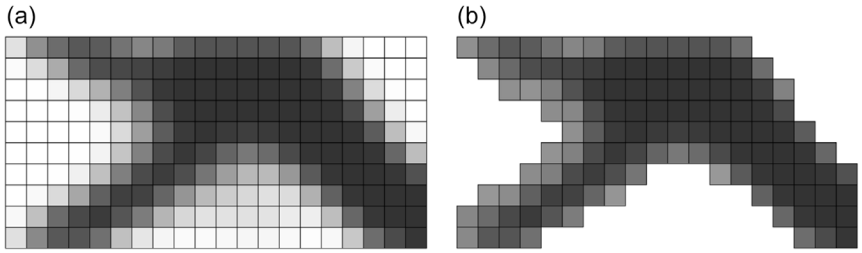

Figure 5. TO of a beam model with density thresholds a) $0.1 < \rho^* < 0.5$ and b) $0.3 < \rho^* < 0.5$.

for reconstructing topology-optimized structures is the RDM method. In this reconstruction process, the primary objective is to populate the topology-optimized design domain with explicitly defined lattice structures. The reconstruction framework (see **Figure 6**) leverages the optimal element density distribution obtained from TO to systematically grade the lattice morphology, thereby ensuring a tailored and optimized lattice structure. To achieve this, an arithmetic averaging technique is employed to compute the average density values of all shared elements, as represented in Equation (7)

$$\rho_{ijk} = \frac{\sum X^*_{ijk}}{N_{\text{node}}} \tag{7}$$

where ρ_{ijk} denotes the computed average density of the node point (i, j, k) located at each element corner and X^*_{ijk} is the density of the elements that share the node point. N_{node} is the number of elements sharing the node as exemplified in Figure 6b. Thus, Equation (7) provides the average mapping density at each element node. Once the density at the element node is known, a linear interpolation method (see Figure 6c) is used to make the grid more precise. This makes it possible for the calculated average densities to be spread out evenly across the elements, which results in a smoother structure. The density of interpolation points can be controlled to have a smooth transition. The reconstructed structure is then exported in .stl format using three-node triangular meshes, as shown in Figure 6d.

This reconstruction algorithm facilitates the generation of both .stl and .fem formats for explicit topology-optimized designs (see **Figure 7**b,c). Similar to the .stl reconstruction, the .fem format employs an alternative meshing approach, utilizing an eight-node hexahedral voxel mesh (see Figure 7b). This format is particularly useful for FEA, enabling the discretization of the design domain into small volumetric elements for accurate mechanical simulations and performance evaluations. Conversely, the STL format transforms the optimized lattice design into a series of

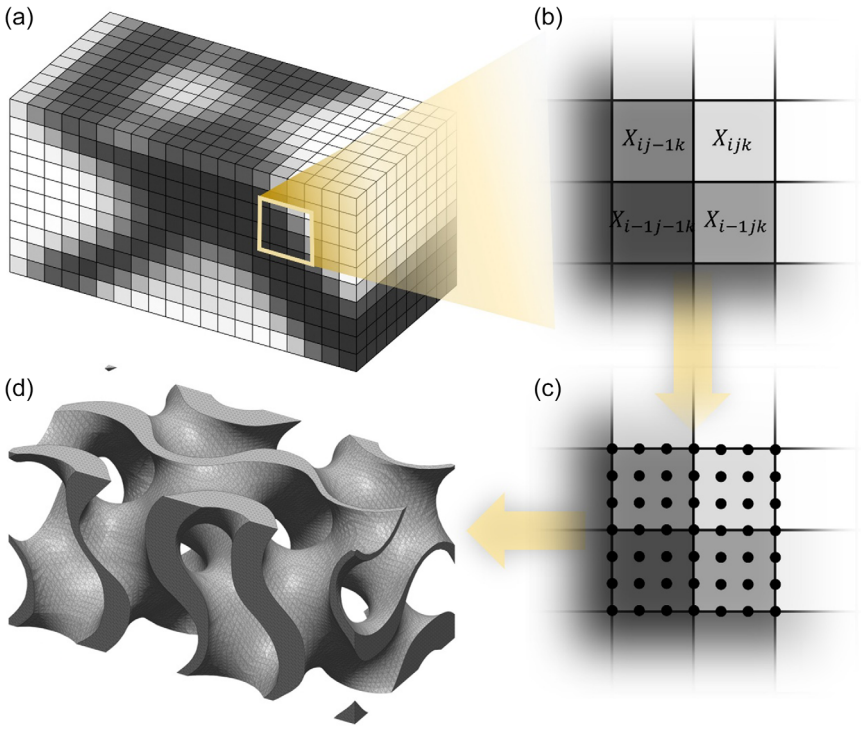

Figure 6. a) Element densities from TO analysis, b) averaging method for a boundary node, c) node enrichment for a smooth reconstruction, and d) reconstructed graded gyroid structure.

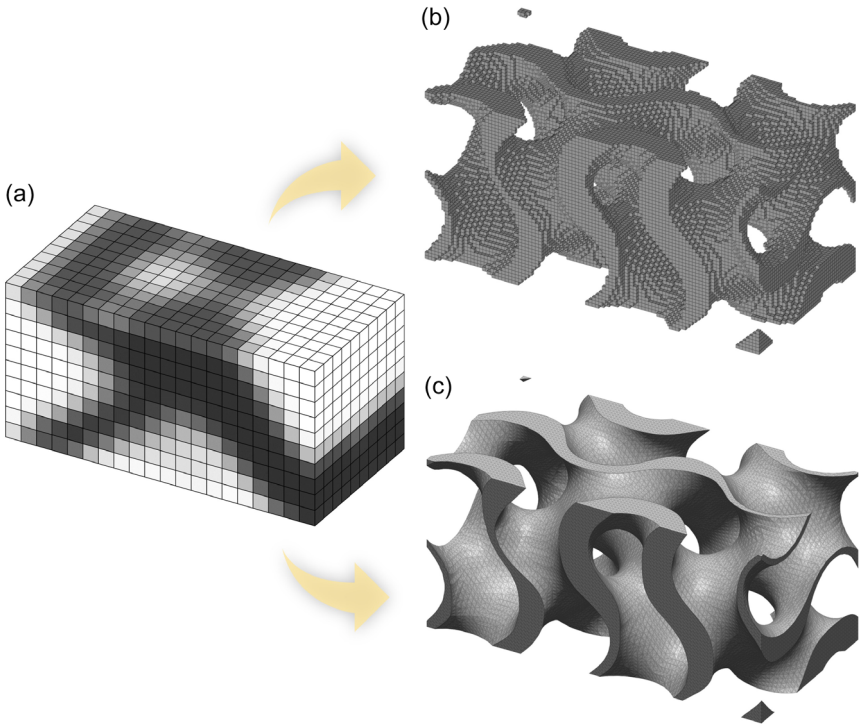

Figure 7. a) TO result, b) reconstructed model in voxel form, and c) reconstructed model in STL form.

interconnected 2D surfaces suitable for AM. By integrating both voxel-based and STL meshing strategies, the reconstruction methodology bridges the gap between TO and practical implementation, offering a comprehensive framework for deploying topology-optimized lattice structures in real-world applications.

The reconstruction algorithm initially determines material connectivity, excluding plates regarded as nondesign domains. This omission simplifies computational complexity; nevertheless, designers may reintegrate plate parts after TO using CAD software. The optimal material distribution is initially determined within a homogenized design domain, defined by coarse meshes that ensure computational efficiency. To accurately represent the specified lattice design, this coarse mesh is converted into a finer discretized distribution. A linear averaging approach is adopted for RDM, wherein density values obtained from finite element-based TO are systematically interpolated. The averaging function, depicted in the MATLAB script lines 318–334 (see Supporting Information), iterates through the element connectivity data to compute average densities for each node, ensuring a seamless transition from coarse to fine mesh representation while maintaining computational tractability.

The following part of the script is the voxel mesh mapping section, where the focus shifts to translating the fine discretized distribution obtained from the linear averaging approach into a structured voxel mesh format suitable for the full-scale FEA. The MATLAB script lines 363–394 (Supporting Information) outlines the iterative process involved in mapping the voxel mesh elements. First, all voxel elements that fall within the TPMS surface are extracted from the distance field domain. Then, each iteration computes the index corresponding to the voxel's position within the filtered fine mesh and generates connectivity information for the voxel element. The resulting voxel mesh elements are then appended with the necessary identifiers and exported into the Altair Optistruct file format.fem for further analyses using commercial tools. This mapping process ensures the conversion of the optimized lattice design into a format compatible with FEA software, facilitating accurate mechanical simulations and performance evaluations.

In the STL generation section, including script lines 355–362 (see Supporting Information), the script utilizes the isosurface and isocaps functions to extract the surface geometry of the fine discretized lattice structure. This geometry is then combined and exported as an STL file using MATLAB stock functions that utilize the well-known marching cubes method from the literature.[68] In summary, the marching cubes method iteratively moves through cubes in the distance field domain and builds the STL from a lookup table of triangles upon checking the corner nodes. By employing these functions, the script efficiently converts the optimized lattice design into the STL format, which is the standard AM application. This facilitates its utilization in AM processes and allows further geometric analysis to be conducted on commercial tools for assessing readiness for manufacturing.

4. Numerical Examples

In order to verify the accuracy of the proposed methodology and script, three distinct optimization cases have been thoroughly examined and experimentally confirmed. The boundary conditions for each case are carefully designed to correspond with the experimental capabilities, taking into account the need for testability. The material RGD720, which has an elastic modulus

of 2100 MPa and a Poisson's ratio of 0.42, is consistently used in all models.[69] Although the specific boundary conditions are explained in the following section for each case study, there are certain conditions that are consistent across all examples. In all instances, the design domains (Ω) are divided into N finite elements, with each element having a relative density between 0.1 and 0.5, represented as $0.1 \leq \rho^* < 0.5$. The targeted volume fraction V for the overall design domain is established as 0.3. Furthermore, the analysis's convergence history is guided by prescribing an initial uniform relative density of 0.2 for each element. The global stiffness matrix K is determined by the material properties of the elements, which depend on their relative densities (i.e., $K = K(\rho^*)$). Consequently, the equation for the steady-state equilibrium is given as follows

$$K(\rho^*)u = f \tag{8}$$

where u and f refer to the global displacement vector and loading vector, respectively. The optimization problem, which minimizes the compliance, is expressed as follows

$$\begin{aligned} &\min_{u \epsilon U, \rho_r} c(\rho^*) = u^T K(\rho^*) u = \sum_{e=1}^{N} u_e^T k_e(\rho^*) u_e \\ &s.t. K(\rho^*)u = f; \\ &0 \leq \rho_{\min} \leq \rho^* \leq \rho_{\max} \leq 1 \\ &\sum_{e=1}^{N} \rho^* \nu_e = V; \end{aligned} \tag{9}$$

where $c(\rho^*)$ refers to minimum compliance. The optimization parameters are also summarized in **Table 5**. The subsequent phase will entail the application of the proposed code to practical case studies, where its performance in commonly used case studies will be assessed. These case studies serve as valuable opportunities to validate the accuracy and effectiveness of the developed code. Through the systematic examination of these case studies, insights into the code's behavior and its applicability across different contexts will be gained, thus contributing to a comprehensive understanding of its capabilities and limitations.

4.1. MBB Beam

The Messerschmitt–Bölkow–Blohm (MBB) beam case that is quintessential to TO literature has been selected for the initial trials. Employing a 1 mm mesh size, the design domain is half of the full MBB beam, leveraging symmetry. Utilizing a P-type lattice (see Table 1) with a 14 mm unit-cell size, the symmetry model incorporates $10 \times 3 \times 3$ unit cells, translating to $20 \times 3 \times 3$ unit-cells into the full model. The overall dimensions of the half-symmetry lattice structure are set at $140 \times 42 \times 42$ mm. At the top and bottom faces of the beam, 1 mm thick plates are used to enhance the testability of the beam. However, the relative density of the plate elements is set to 1 because the plates are defined as non-design domains. A roller-type boundary condition ($U_y = 0$) is applied through a line at $x = 20$ mm, while a symmetry boundary condition ($U_x = 0$) is imposed on a plane at $x = 140$ mm. The total load in the symmetry model is set to be 500 N and applied on a line distribution at the edge of the symmetry plane. The default boundary conditions of the proposed MATLAB script are established as the symmetry MBB beam test case illustrated in script lines 35–44 (Supporting Information). Here, it is important to note that the applied load is evenly distributed on the edge of the symmetry plane. The schematic view of the boundary conditions and load are illustrated in **Figure 8**.

After establishing the design parameters and boundary conditions for the MBB beam optimization example, the TO process is executed, and the resulting optimal material distribution is displayed in **Figure 9**. In order to perform a comprehensive assessment, a uniform P-type lattice design is also generated without optimization and examined under identical conditions. The compliance value for the uniform lattice design is determined to be 680.97 mm N^{-1}, whereas the optimized graded lattice design achieves a compliance value of 468.44 mm N^{-1}. The substantial disparity of 31.2% highlights the exceptional efficiency of the

Table 5. Design variables of TO cases.

Constraints of TO
Element minimum density, $\rho_{min} = 0.1$
Element maximum density, $\rho_{max} = 0.5$
Element initial density, $\rho_{initial} = (\rho_{min} + \rho_{max})/2$
Total volume, $V = 0.3$
Objective of TO
Minimize compliance, $\min(c(\rho^*))$

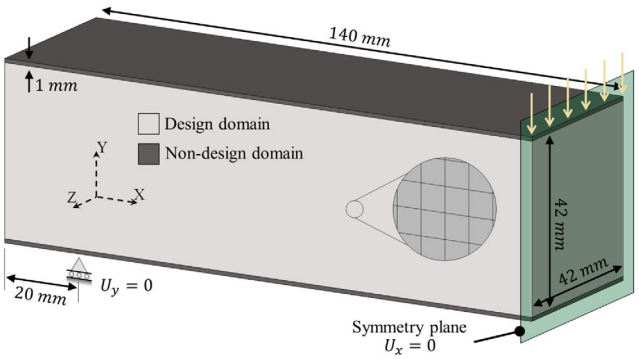

Figure 8. A schematic view of the half-symmetry MBB beam case.

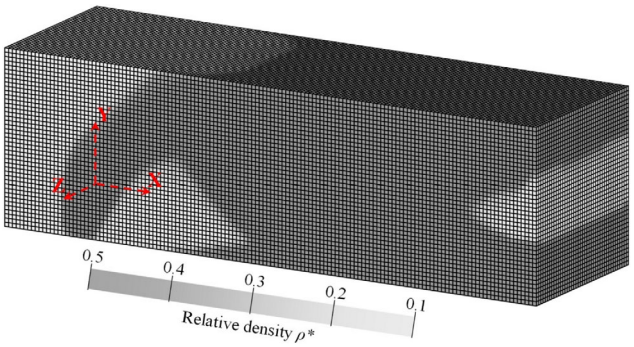

Figure 9. The element density distribution for the half-symmetry MBB beam case (plates are excluded for better visualization).

optimized FGL construction. The observed improvement in structural performance is notably influenced by the distribution of material along the loading direction. The effectiveness of the suggested FGL structure in optimizing the MBB beam configuration is highlighted, demonstrating the power of morphological grading even in lattice structures that are fundamentally better than uniform designs.

Following the completion of the TO phase for the MBB beam case, the subsequent step involves the reconstruction of the topologically optimized design. The reconstructed voxel model is explicitly illustrated in **Figure 10**a. The omission of plates in the reconstructed model enhances the clarity of lattice morphology grading. Identical boundary conditions to those applied during TO are used (see Figure 8) to evaluate the accuracy of the full-scale reconstructed finite element model. The displacement results and compliance values are then compared with the final iteration of the TO. The total compliance of the TO is determined by multiplying the compliance value of the symmetry model for the TO by two, resulting in a value of 936.88 mm N^{-1}. Conversely, the total compliance of the reconstructed geometry is calculated as 1088.37 mm N^{-1}, yielding a relative difference of 16.2%. The relative error here is relatively large and may not be deemed reasonable for engineering applications. To comprehend the source of the error, the models are evaluated by plate and design domain compliances separately. The compliances for the design domain and plates of the TO design are 616.26 and 320.62 mm N^{-1}, respectively. In contrast, for the reconstructed geometry, the compliances are calculated as 608.23 and 480.14 mm N^{-1} for the design domain and plates, respectively. The compliance ratio of the design domain to plates is 0.52 and 0.79 for the TO and reconstructed design, respectively. Consequently, the relative errors are 1.3% and 27.3% for the design domain and plates, respectively. Notably, a significant local deformation of the plate at symmetry (see Figure 10b), where the load is applied, is observed. This is attributed to the explicit form of the P-type lattices, where no elements exist on the edges. The second parameter for comparison is the displacement in the *y*-direction value at the symmetry plane. The average displacement, which is calculated on the line of force load applied location, is calculated as −1.8081 and −2.0264 mm for TO and reconstructed geometries, respectively, resulting in a relative error of 12.1%, largely due to the local deformation of the top plate at the symmetry plane. The comparison results of MBB beam cases for the TO, uniform, and reconstructed geometry obtained from the TO results are tabulated in **Table 6** for full model.

Following the thorough validation of the accuracy of the reconstructed geometries for the MBB beam case, the structure is now

Table 6. Comparative results for the MBB beam case.

	c [mm N^{-1}]	Relative difference [%]	U_{y_mean} [mm]	Relative difference [%]
TO	936.88	–	−1.81	–
Uniform	1361.94	31.2	−2.60	30.6
Reconstructed	1088.38	16.2	−2.03	12.1

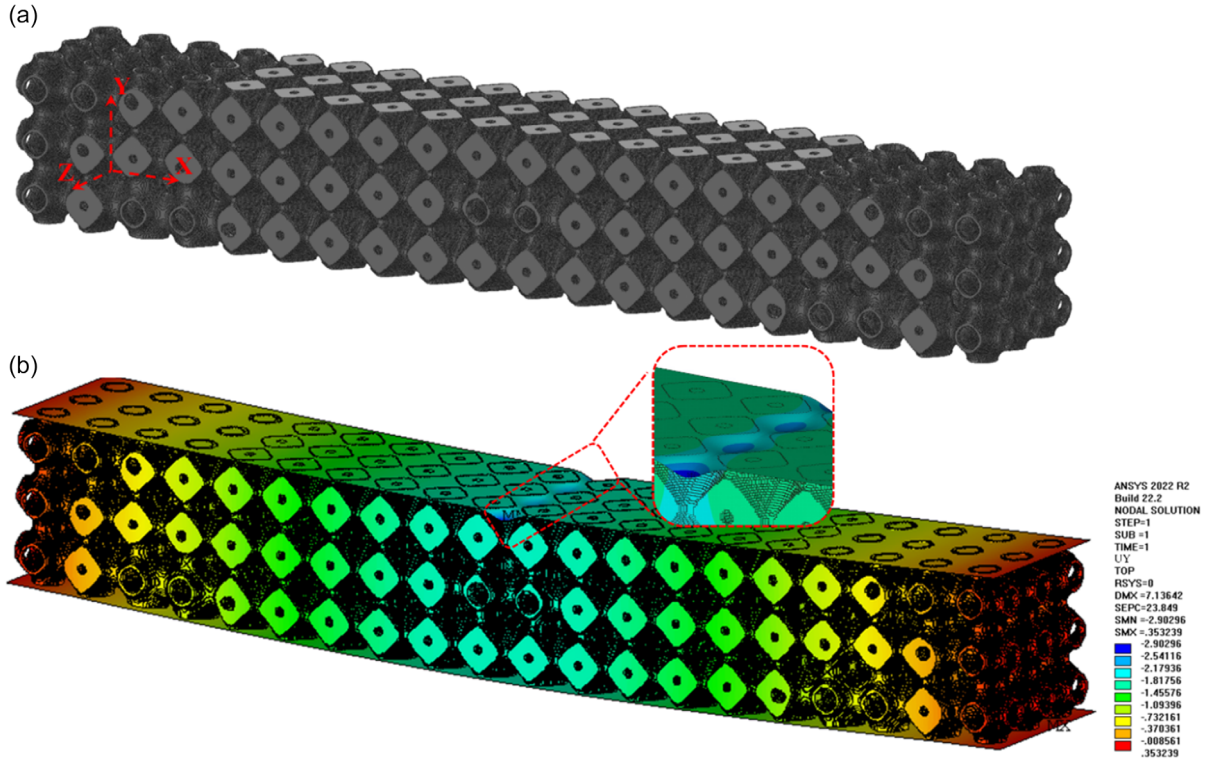

Figure 10. a) Reconstructed MBB voxel model and b) FEA displacement results.

ready for the AM phase. The export of structures in STL format, as illustrated in **Figure 11**, is a pivotal step in this process. A precautionary check is conducted, confirming a total relative density of 0.3 for the design domain. This meticulous verification ensures that the exported file aligns precisely with specifications, signifying the structure's readiness for the upcoming AM process.

4.2. Cantilever Beam

Another case that is prevalent in the TO literature is the cantilever beam problem. The dimensions of the design domain are specified as $132 \times 36 \times 36$ mm, and the material properties of the lattice structure are based on G-type lattice (see Table 2) with a unit-cell size of 12 mm. Therefore, the overall dimensions of the unit-cell for this scenario are 11 units in the x-direction, three units in the y-direction, and three units in the z-direction. The design domain is discretized using eight-node hexahedral elements, each with a mesh size of 1 mm. Furthermore, the top and bottom plates are included in the model; however, they are designated as nondesign domains. In this cantilever beam configuration, the right top and bottom plates are fixed in planes at $y = 0$ and $y = 38$ mm with dimensions $x = 0$–12 and $z = 0$–36 mm, effectively constraining a clamped boundary condition on a unit-cell size (12 mm) in the x-direction. In order to apply the load, a total force of 500 N is evenly distributed along a line on the top plane, with a distance of 120 mm from the top plate and perpendicular to it. **Figure 12** displays the schematic depiction of the cantilever beam case study. The boundary conditions for the study of the cantilever beam are provided in the script lines 418–429 (Supporting Information), and corresponding script lines of the MBB case can be replaced with these to simulate the cantilever beam case. The identical loading condition employed in the MBB beam case is being used.

Following the establishment of design parameters and boundary conditions for the cantilever beam optimization case, the TO process is initiated, and the resulting material distribution is presented in **Figure 13**. In order to provide a comprehensive analysis, a uniform G-type lattice design is examined under identical conditions. The compliance value for the uniform lattice design is determined to be 732.23 mm N^{-1}, while the compliance value for the optimized graded lattice design converges to 563.47 mm N^{-1}. Evidently, the graded lattice design outperforms the uniform design by a significant margin of 23.0%.

After the conclusion of the TO phase for the cantilever beam, the subsequent step involves the reconstruction of the topologically optimized design. In line with the specified material properties for the G-type lattice, the structure is reconstructed explicitly and illustrated in **Figure 14**a. To enhance the clarity of lattice morphology grading, the plates are intentionally omitted in the reconstructed model. Identical boundary conditions to those applied during TO are used to assess the accuracy of the reconstructed model. The displacement results (see Figure 14b) and compliance values are then compared with the final iteration of the TO. The compliance value at the final iteration of the TO is determined to be 563.47 mm N^{-1}. In contrast, it is calculated as 576.04 mm N^{-1} for the reconstructed geometry, resulting in a relative difference of 2.2%. An average displacement in the loading direction (U_{y_mean}) is also considered for comparison. The average displacement on a y–z plane at the loading location ($x = 120$ mm) for TO is calculated as -2.224 mm, whereas for the reconstructed geometry, it is -2.241 mm. Consequently, the relative error in this case is calculated as 0.8%. These comparisons provide insights into the accuracy and effectiveness of the reconstruction method and script. The comparison results of cantilever beam cases are tabulated in the **Table 7**.

Having validated the accuracy of the reconstructed geometries for the cantilever beam case, the structure is now poised for AM. The export of structures in STL format, as shown in **Figure 15**, is followed by a precautionary check, confirming a total relative density of 0.3 for the design domain. This verification ensures the exported file precisely aligns with specifications, confirming the structure's readiness for the AM process.

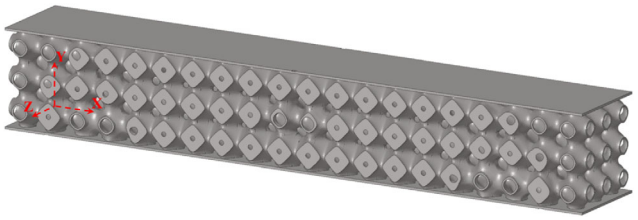

Figure 11. Full model of optimized MBB beam case in STL format.

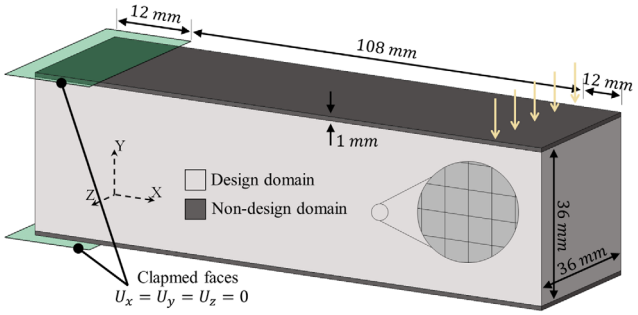

Figure 12. A schematic view of the cantilever beam case.

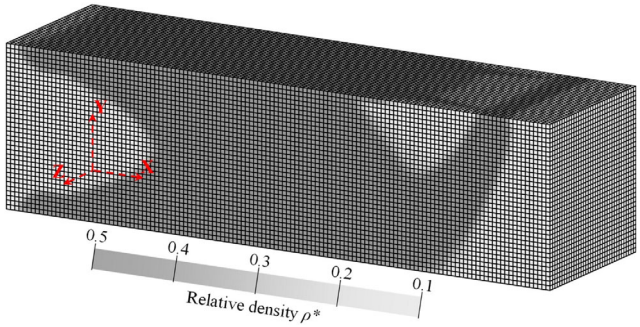

Figure 13. The element density distribution for the cantilever beam case (plates are excluded for better visualization).

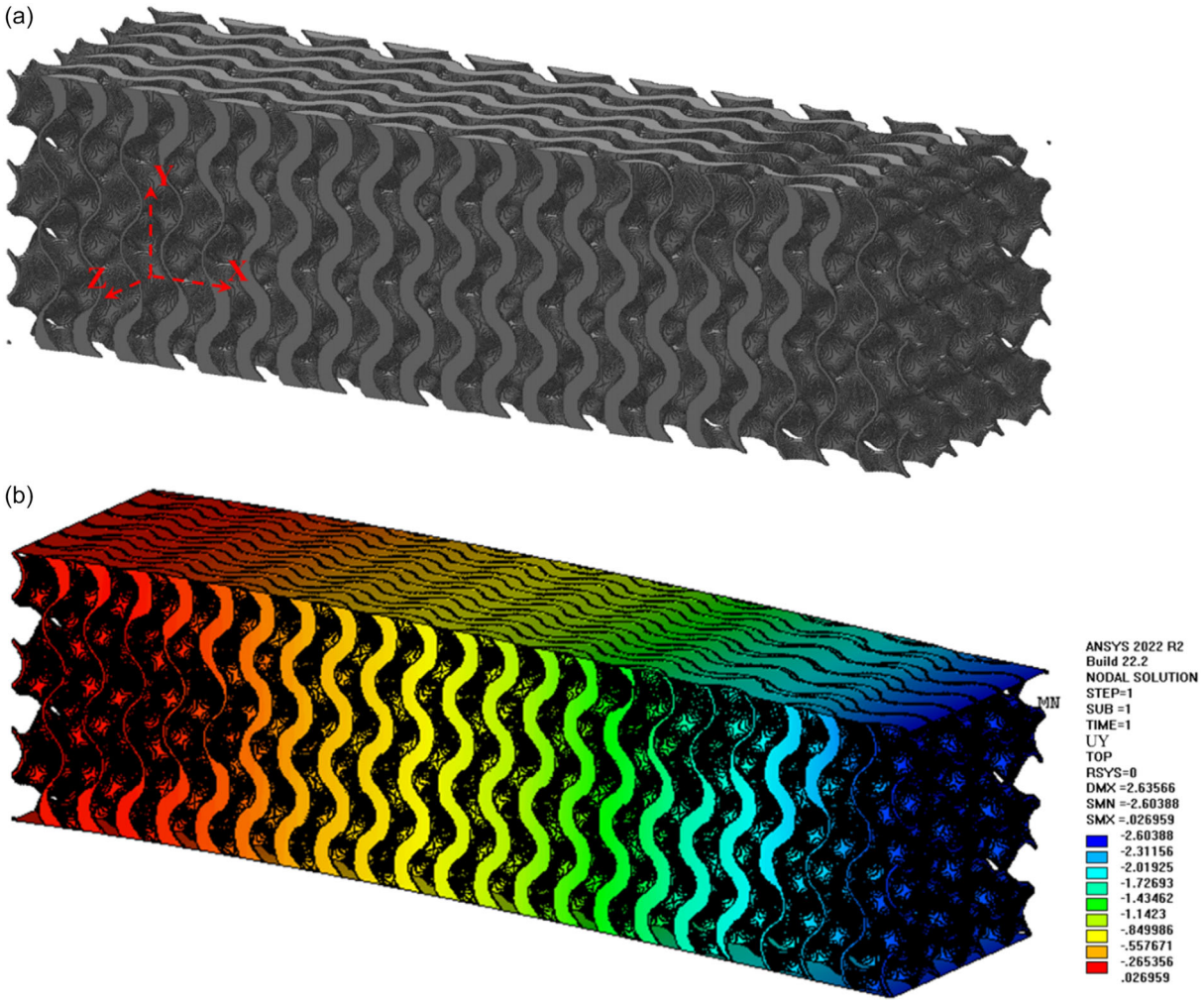

Figure 14. a) Reconstructed cantilever voxel model and b) FEA displacement results.

Table 7. Comparative results for the cantilever beam case.

	c [mm N^{-1}]	Relative difference [%]	U_{y_mean} [mm]	Relative difference [%]
TO	563.47	–	−2.22	–
Uniform	732.23	23.0	−2.89	23.0%
Reconstructed	576.04	2.2	−2.24	0.8

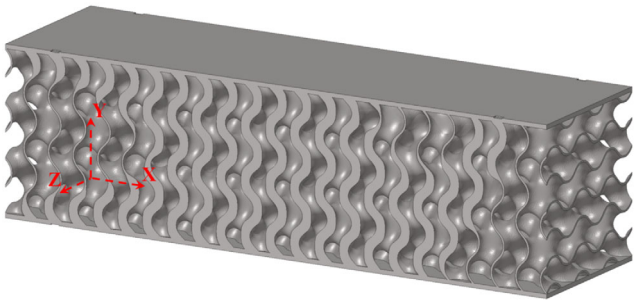

Figure 15. Reconstructed cantilever beam case in STL format.

4.3. Flatwise Compression

As a final case, the aim of providing a TO to improve the compression performance of the proposed structure is chosen as it can provide lucrative engineering opportunities. Accordingly, this study employs a flatwise compression case study to evaluate the proposed code. The design domain has dimensions of $60 \times 60 \times 60$ mm, and the anisotropic material properties, represented by the curves C_{11}, C_{12}, and C_{44}, are specifically designed for D-type lattices (see Table 2). The unit-cell size for the D lattice is set to be 12 mm, resulting in a total of $5 \times 5 \times 5$ unit cells within the design domain. To discretize the design domain, a mesh size of 1 mm is utilized, employing eight-node hexahedral elements with three degrees of freedom at each node. The design domain is flanked by top and bottom plates, both designated as nondesign domains, maintaining a constant relative density of 1. The bottom plate is rigidly fixed to the ground, while a total flatwise loads of 2 kN is uniformly applied to the top plate in

the *y*-direction. The boundary conditions for the flatwise compression case are detailed in script lines 430–439 (Supporting Information), and the corresponding lines for the MBB case can be replaced with these to model the cantilever beam example.

The schematic representation of the flatwise compression case study is illustrated in the following **Figure 16** for clarity. Upon establishing the design parameters and boundary conditions for the flatwise compression case, the TO process is initiated, and the resulting material distribution is presented in **Figure 17**. To facilitate a comparative analysis with graded structures, a uniform design is examined under identical conditions.

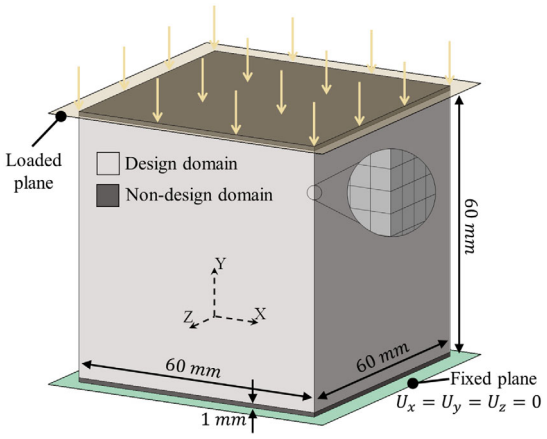

Figure 16. A schematic view of the flatwise compression case.

The compliance value for the uniform design is determined to be 114.89 mm N^{-1}, whereas the compliance value for the graded design converges to 104.16 mm N^{-1}. Notably, the graded design exhibits superior performance, surpassing the uniform design by 9.3%. This observation underscores the effectiveness of the proposed graded structure in enhancing the structural performance under flatwise compression conditions.

Following the completion of the TO phase, the subsequent step involves reconstructing the topologically optimized design for further FEA and fabrication. The reconstructed and sandwiched structure with plates is illustrated in **Figure 18**a. The omission of the plates in the reconstructed model is intentional, aimed at enhancing the clarity of the lattice morphology grading. To assess the accuracy of the reconstructed model, identical boundary conditions as those in the TO phase are applied. The compliance values and displacement results (see Figure 18b) are then compared with the final iteration of the TO. Specifically, the compliance values are determined as 104.16 and 105.91 mm N^{-1} for TO and reconstructed geometries, respectively, resulting in a relative error of 1.7%. This discrepancy is considered accurate enough for the majority of engineering applications. It is pertinent to note that, due to the local deformation characteristics of the discontinuous lattices, an average displacement at the top plate is calculated and compared with the values from the topology-optimized and reconstructed geometries. The second parameter for comparison is the average displacement in the loading direction at the top plates, yielding values of −0.1042 and −0.1040 mm for TO and reconstructed geometries, respectively. A similar 0.2% error is calculated here, associated with the same considerations as in

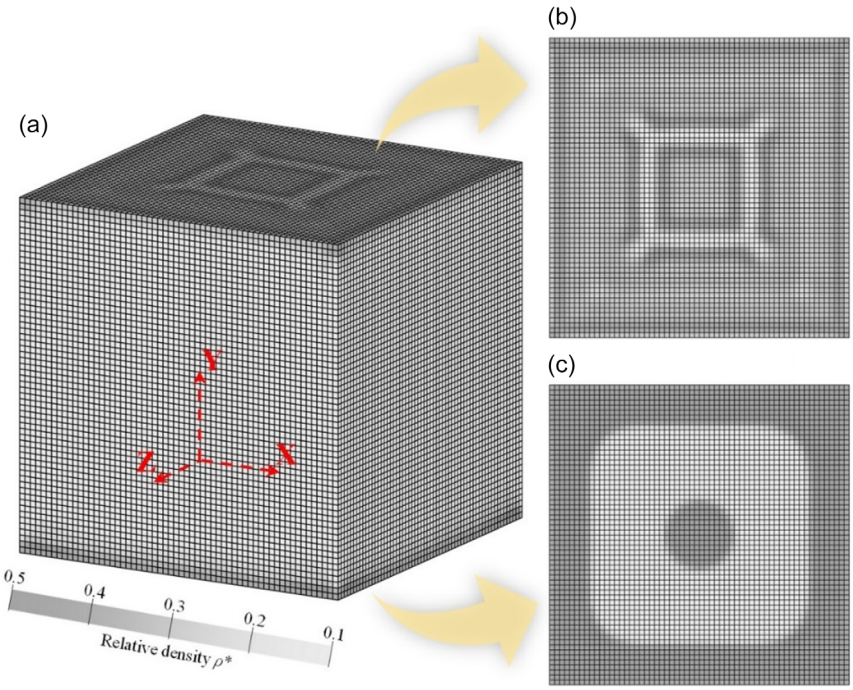

Figure 17. The element density distribution for the flatwise compression case a) iso, b) top, and c) bottom views (plates are excluded for better visualization).

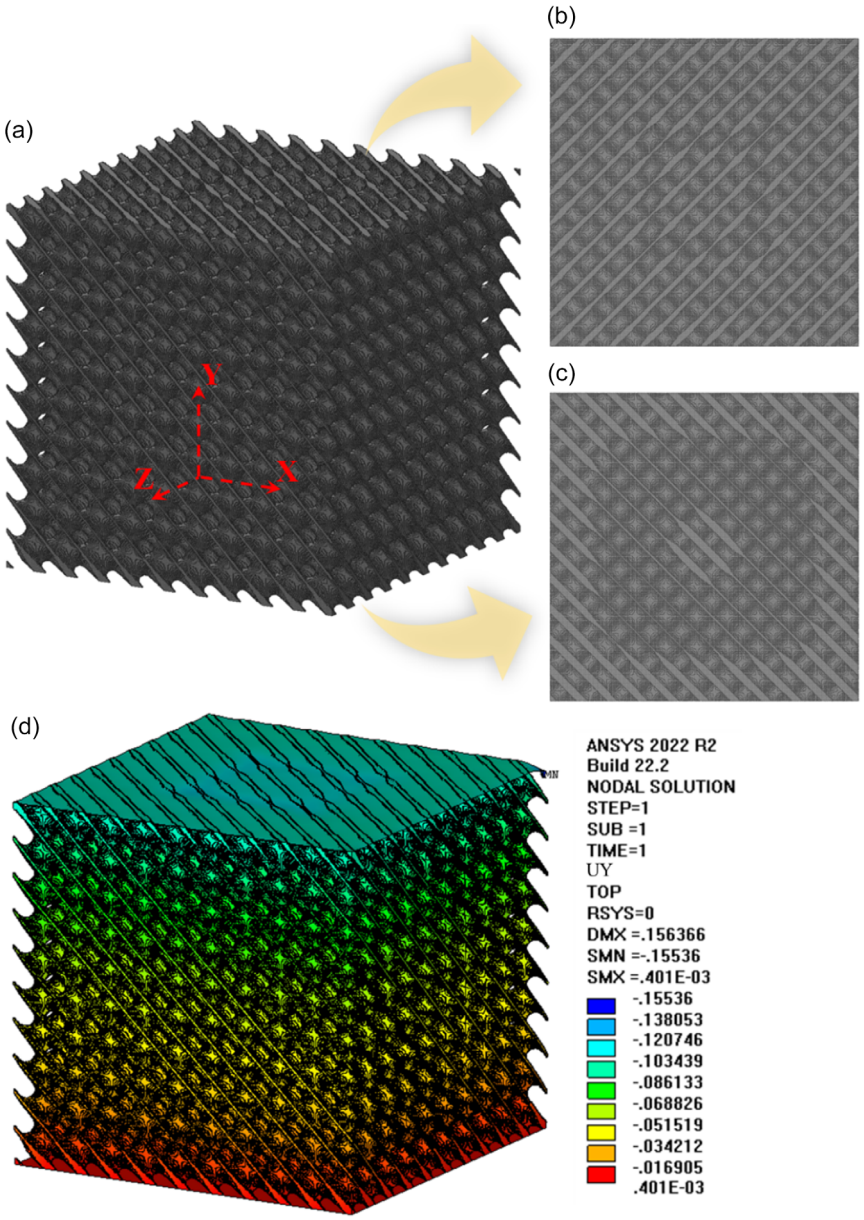

Figure 18. Reconstructed flatwise compression voxel model views a) iso, b) top, c) bottom view, and d) FEA displacement results.

compliance assessment. The comparative results of the flatwise compression case are tabulated in **Table 8**.

After confirming the accuracy of the reconstructed geometries, the structure is prepared for AM. To facilitate this, the structures are exported in STL format, as illustrated in the following **Figure 19**. As a precautionary step, the total relative density of the STL-formatted structure is verified, and it is determined to be 0.3 for the design domain. This verification ensures that the exported file aligns with the desired specifications, reinforcing the readiness of the structure for the AM process.

Table 8. Comparative results for the flatwise compression case.

	c [mm N^{-1}]	Relative difference [%]	U_{y_mean} [mm]	Relative difference [%]
TO	104.16	–	−0.1042	–
Uniform	114.89	9.3	−0.1149	9.3
Reconstructed	105.91	1.7	−0.1040	0.2

The comprehensive analyses of the flatwise compression, cantilever beam, and MBB beam configurations have provided valuable insights into the performance and accuracy of the proposed optimization code. From the initiation of TO to the reconstruction of optimized designs and their readiness for AM, each step has been scrutinized. The observed enhancements in structural performance underscore the efficacy of the proposed graded lattice structures, highlighting their potential in diverse engineering applications.

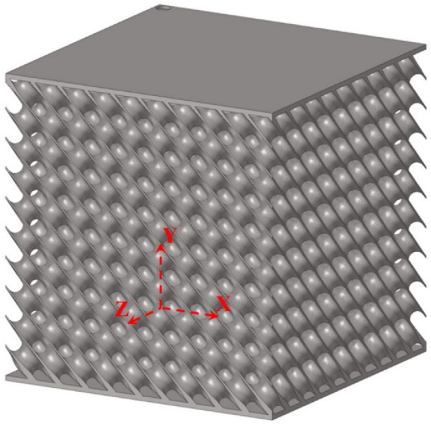

Figure 19. Reconstructed flatwise compression case in STL format.

5. Fabrication and Experimental Validation

To validate the results of the proposed method with testing equipment, the graded designs were printed using the material jetting AM modality. In the material jetting process, photopolymer materials are heated and deposited on a build plate layer by layer, and then in each layer, ultraviolet light is used to cure the molten material.[70,71] All three optimization cases were validated by experiments. Stratasys Objet Connex 1 machine was used to build the graded geometries (see **Figure 20**). During the build process, a 16 μm layer thickness with a high-quality printing mode was used. Transparent RGD720 material and soluble solution SUP706B material were used as the main and the support materials, respectively. Once the production was completed, the support material inside the printed lattice structures were removed by using a sodium hydroxide (NaOH) solution.

The printed specimens are then tested under different loading scenarios. To compare the numerical results with the experiments, force versus displacement graphs were drawn from both numerical analyses and experiments. These analyses were performed with elastic material properties, and no plasticity was considered. Therefore, only the linear region of the force–displacement graphs was investigated for comparison. First, a 3-point test was performed for the printed P-type FGL structure. In all tests, MTS universal testing machine (MTS 322 test frame) with a 100 kN load cell was utilized. The 3-point flexural test was conducted according to ASTM D 760, and all specimens were tested at a constant loading rate of 1 mm min^{-1}. The 3-point bending test set-up and force–displacement results are presented in **Figure 21**. The bending stiffness values (slope of the force–displacement curve) are calculated as 492.6 and 476.0 N mm^{-1} for the simulation and experiment, respectively, in the linear regions using a MATLAB code. The relative error between the experiment and the numerical simulation is 3.5%, which confirms a good agreement between the simulation and experimental results.

Furthermore, a test on the cantilever-beam specimen was also conducted using the identical test configuration depicted in **Figure 22**a. The boundary conditions employed in the experiment were the same as those utilized in FEA. Figure 22b displays the force–displacement graph for both the simulation and the experimental results. The simulation previously provided the average displacement value obtained from force-applied nodes, which was documented in Table 7. However, based on the

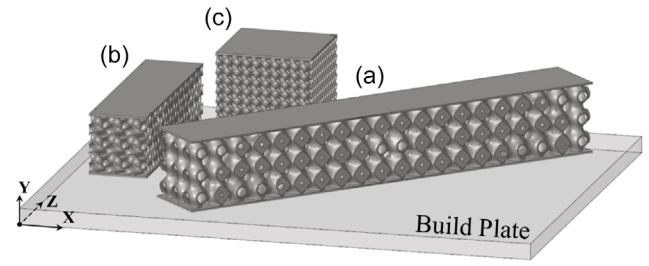

Figure 20. Build layout for a) MBB, b) cantilever beams, and c) compression specimens.

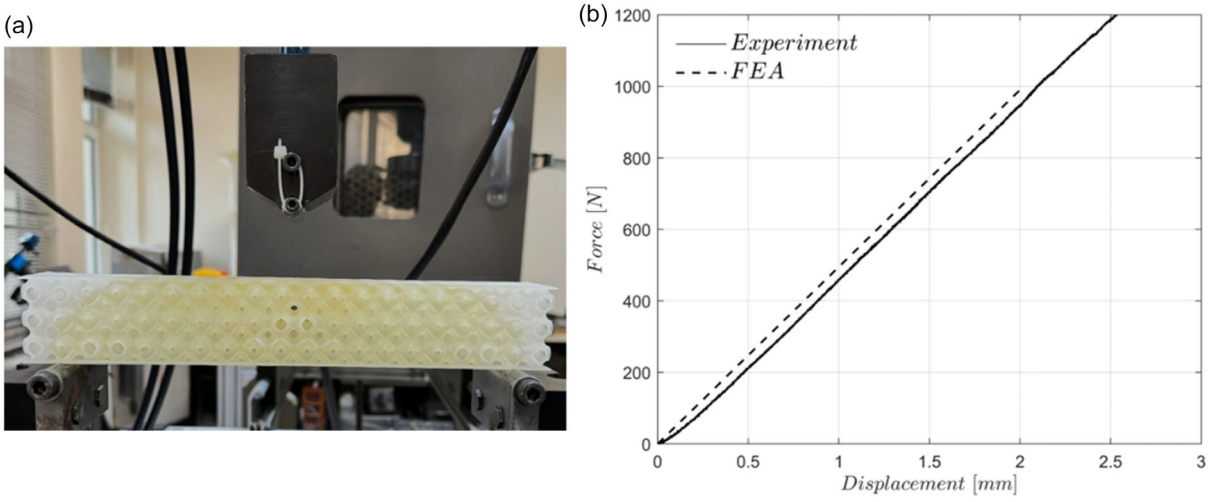

Figure 21. a) Fabricated MBB-beam specimen test set-up and b) force–displacement graph.

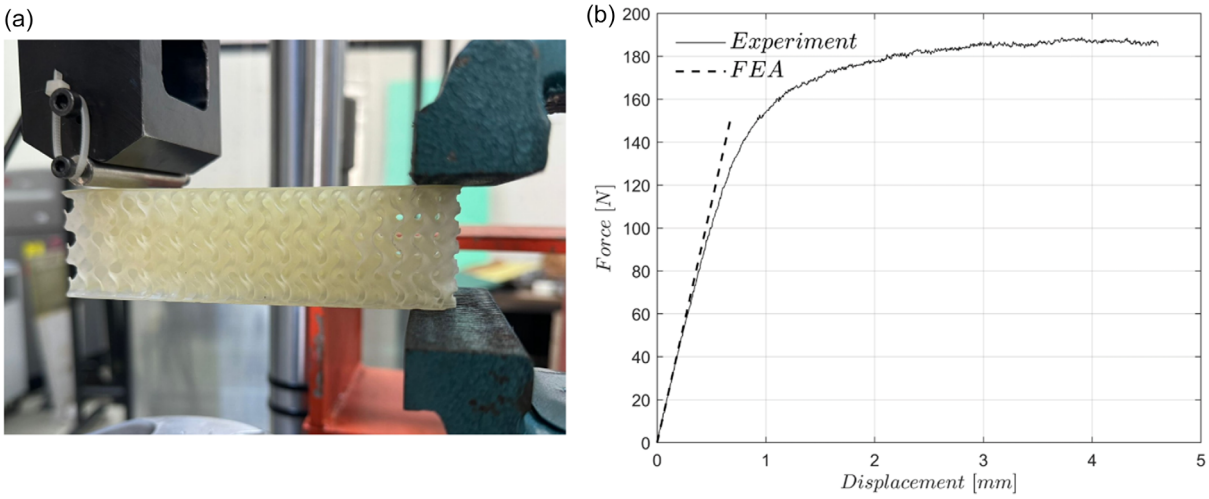

Figure 22. a) Fabricated cantilever-beam specimen test set-up and b) force–displacement graph.

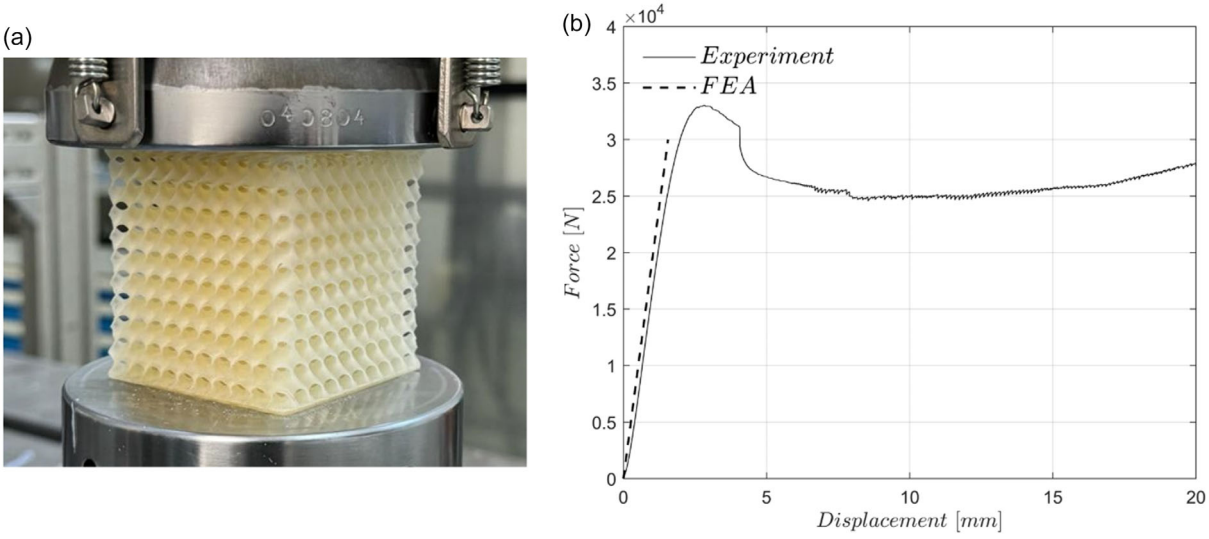

Figure 23. a) Fabricated flatwise compression specimen test set-up and b) force–displacement graph.

experimental findings, it has been shown that a force of 500 N exceeds the linear range. Consequently, the average displacement value obtained from FEA was proportionally adjusted to match the force value of 150 N. The flexural stiffnesses for the simulation and experiment were determined to be 223.2 and 210.0 N mm^{-1}, respectively. The relative error, which measures the discrepancy between the experiment and the numerical simulation, is 6.3%. This indicates a strong agreement between the simulation and experimental data.

The final experiment was conducted on a flatwise compression specimen to verify the proposed code. **Figure 23**a,b illustrates the instrumentation and force–displacement graphs that were obtained from the FEA and the test, respectively. The slope of the force–displacement curve was determined to be 19230.8 N mm^{-1} for the FEA and 18236.7 N mm^{-1} for the experiment, respectively. The numerical simulation and the experiment have a discrepancy of 5.3%. This implies that the simulation and experimental data are in firm agreement, as evidenced by the same results in the previous cases.

6. Conclusions

The findings of our research demonstrate encouraging results for the use of the developed code in commonly used case studies. The effectiveness of graded lattice structures in improving structural performance has been proven by thorough analysis of MBB beam, cantilever beam, and flatwise compression configurations. The proposed MATLAB code, which combines homogenization-based TO with a reconstruction technique, provides researchers with a distinct solution to evaluate their concept for creating FGL structures to take full advantage of AM. The TO approach consistently produced material distributions in each case study that were much better than uniform designs, demonstrating the

superiority of graded structures. Moreover, the precision and practicality of our method were validated by reconstructing these optimized designs and subsequently evaluating them against the TO results. Although there were some small differences due to factors like curve fitting and mesh resolution, the reconstructed geometries had relative errors that were within acceptable ranges for engineering purposes. The method was further supported by fabrication and experimental validation, which demonstrated its potential. Graded geometries for all specimens were successfully fabricated utilizing AM. The experimental testing produced findings that nearly matched the numerical calculations, confirming the accuracy of our approach. The observed deviations can be related to changes in the dimensions of the printed specimens and discrepancies in material characteristics. In summary, our study emphasizes the significant impact of homogenization-based TO and reconstruction algorithms on lattice structure design and fabrication. These algorithms help bridge the gap between theoretical concepts and practical applications, hence enhancing engineering optimization skills.

Supporting Information

Supporting Information is available from the Wiley Online Library or from the author.

Acknowledgements

This research is supported by the Scientific and Technological Research Council of Turkey (TUBITAK) 2219 – International Postdoctoral Research Fellowship Program.

Conflict of Interest

The authors declare no conflict of interest.

Author Contributions

Mirhan Ozdemir: conceptualization (equal); methodology (equal); software (equal); validation (equal); visualization (equal); writing—original draft (lead); and writing—review and editing (equal). **Ugur Simsek**: conceptualization (lead); investigation (lead); methodology (lead); software (equal); supervision (lead); validation (lead); visualization (equal); writing—original draft (equal); and writing—review and editing (lead). **Cemal Efe Gayir**: methodology (equal); software (lead); validation (equal); visualization (lead); and writing—original draft (supporting). **Kadir Gunaydin**: investigation (equal); validation (equal); writing—original draft (equal); and writing—review and editing (supporting). **Orhan Gulcan**: investigation (supporting); validation (equal); writing—original draft (equal); and writing—review and editing (supporting).

Data Availability Statement

The data that support the findings of this study are available on request from the corresponding author. The data are not publicly available due to privacy or ethical restrictions.

Keywords

functionally graded lattices, homogenization, lattice generation, topology optimization, triply periodic minimal surface

Received: November 3, 2024
Revised: May 22, 2025
Published online: July 4, 2025

[1] X. Z. Zhang, M. Leary, H. P. Tang, T. Song, M. Qian, *Curr. Opin. Solid State Mater. Sci.* **2018**, *22*, 75.
[2] T. Maconachie, M. Leary, B. Lozanovski, X. Zhang, M. Qian, O. Faruque, M. Brandt, *Mater. Des.* **2019**, *183*, 108137.
[3] B. Sokollu, O. Gulcan, E. I. Konukseven, *Addit. Manuf.* **2022**, *60*, 103199.
[4] M. Naebe, K. Shirvanimoghaddam, *Appl. Mater. Today* **2016**, *5*, 223.
[5] V. A. Popovich, E. V. Borisov, A. A. Popovich, V. S. Sufiiarov, D. V. Masaylo, L. Alzina, *Mater. Des.* **2017**, *114*, 441.
[6] B. Stoner, J. Bartolai, D. V. Kaweesa, N. A. Meisel, T. W. Simpson, *JOM* **2018**, *70*, 413.
[7] E. Sanchez-Palencia, *Lecture Notes in Mathematics*, Vol. *985*, Springer, Berlin **1983**.
[8] A. Bensoussan, L. Lions, G. Papanicolaou, *Studies in Mathematics and Its Application*, Vol. *5*, North-Holland, Amsterdam **1978**.
[9] I. Babuška, in *Proc. of the Third Symp. on the Numerical Solution of Partial Differential Equations*, SYNSPADE 1975, Held at the University of Maryland, College Park, MD, May **1975**, p. 89.
[10] R. Rishmany, C. Mabru, R. Chieragatti, F. R. Aria, *Int. J. Mech. Sci.* **2008**, *50*, 1114.
[11] S. Arabnejad, D. Pasini, *Int. J. Mech. Sci.* **2013**, *77*, 249.
[12] K. Wang, M. Cai, P. Zhou, G. Hu, *Struct. Multidiscip. Optimiz.* **2021**, *64*, 3911.
[13] A.-J. Wang, D. L. McDowell, *J. Eng. Mater. Technol.* **2004**, *126*, 137.
[14] N. Staszak, T. Garbowski, A. Szymczak-Graczyk, *Materials* **2021**, *14*, 4120.
[15] Y. Chen, X. N. Liu, G. K. Hu, Q. Sun, Q. S. Zheng, *Proc. R. Soc. A* **2014**, *470*, 20130734.
[16] A. Vigliotti, D. Pasini, *Mech. Mater.* **2012**, *46*, 57.
[17] J. Somnic, B. W. Jo, *Materials* **2022**, *15*, 605.
[18] R. Yang, A. Chahande, *Struct. Optimiz.* **1995**, *9*, 245.
[19] X. Wang, S. Xu, S. Zhou, W. Xu, M. Leary, P. Choong, M. Qian, M. Brandt, Y. M. Xie, *Biomaterials* **2016**, *83*, 127.
[20] J. H. Zhu, W. H. Zhang, L. Xia, *Arch. Comput. Methods Eng.* **2016**, *23*, 595.
[21] L. L. Beghini, A. Beghini, N. Katz, W. F. Baker, G. H. Paulino, *Eng. Struct.* **2014**, *59*, 716.
[22] M. P. Bendsøe, *Struct. Optimiz.* **1989**, *1*, 193.
[23] Y. Tang, A. Kurtz, F. Y. Zhao, *Comput.-Aided Des.* **2015**, *69*, 91.
[24] J. Liu, H. Yu, A. C. To, *Struct. Multidiscip. Optimiz.* **2018**, *57*, 849.
[25] B. Zhu, X. Zhang, H. Zhang, J. Liang, H. Zang, H. Li, R. Wang, *Mech. Mach. Theory* **2020**, *143*, 103622.
[26] J. Wu, O. Sigmund, J. P. Groen, *Struct. Multidiscip. Optimiz.* **2021**, *63*, 1455.
[27] M. P. Bendsøe, N. Kikuchi, *Comput. Methods Appl. Mech. Eng.* **1988**, *71*, 197.
[28] J. Plocher, A. Panesar, *Mater. Des.* **2019**, *183*, 108164.
[29] D. Li, N. Dai, Y. Tang, G. Dong, Y. F. Zhao, *J. Mech. Des.* **2019**, *141*, 071402.
[30] L. Cheng, P. Zhang, E. Biyikli, J. Bai, J. Robbins, A. To, *Rapid Prototyping J.* **2017**, *23*, 660.
[31] U. Simsek, C. E. Gayir, G. Kiziltas, P. Sendur, *Int. J. Adv. Manuf. Technol.* **2020**, *111*, 1361.

[32] M. Ozdemir, U. Simsek, G. Kiziltas, C. E. Gayir, A. Celik, P. Sendur, *Addit. Manuf.* **2023**, *70*, 103560.
[33] D. Zhang, X. Zhai, L. Liu, X. Fu, *Struct. Multidiscip. Optimiz.* **2023**, *66*, 207.
[34] O. Sigmund, *Struct. Multidiscip. Optimiz.* **2001**, *21*, 120.
[35] G. Kharmanda, N. Olhoff, A. Mohamed, M. Lemaire, *Struct. Multidiscip. Optimiz.* **2004**, *26*, 295.
[36] V. J. Challis, *Struct. Multidiscip. Optimiz.* **2010**, *41*, 453.
[37] X. Huang, Y. Xie, *Struct. Multidiscip. Optimiz.* **2010**, *41*, 671.
[38] K. Suresh, *Struct. Multidiscip. Optimiz.* **2010**, *42*, 665.
[39] E. Andreassen, A. Clausen, M. Schevenels, B. S. Lazarov, O. Sigmund, *Struct. Multidiscip. Optimiz.* **2011**, *43*, 1.
[40] K. Liu, A. Tovar, *Struct. Multidiscip. Optimiz.* **2014**, *50*, 1175.
[41] R. Tavakoli, S. M. Mohseni, *Struct. Multidiscip. Optimiz.* **2014**, *49*, 621.
[42] Z. H. Zuo, Y. M. Xie, *Adv. Eng. Softw.* **2015**, *85*, 1.
[43] E. Biyikli, A. C. To, *PLoS One* **2015**, *10*, e0145041.
[44] L. Xia, P. Breitkopf, *Struct. Multidiscip. Optimiz.* **2015**, *52*, 1229.
[45] P. Wei, Z. Li, X. Li, M. Y. Wang, *Struct. Multidiscip. Optimiz.* **2018**, *58*, 831.
[46] A. Laurain, *Struct. Multidiscip. Optimiz.* **2018**, *58*, 1311.
[47] R. A. Loyola, O. M. Querin, A. G. Jiménez, C. A. Gordoa, *Struct. Multidiscip. Optimiz.* **2018**, *58*, 1297.
[48] Q. Chen, X. Zhang, B. Zhu, *Struct. Multidiscip. Optimiz.* **2019**, *59*, 1863.
[49] M. Yaghmaei, A. Ghoddosian, M. M. Khatibi, *Struct. Multidiscip. Optimiz.* **2020**, *62*, 1001.
[50] Y. Liang, G. Cheng, *Struct. Multidiscip. Optimiz.* **2020**, *61*, 411.
[51] D. Yago, J. Cante, O. Lloberas-Valls, J. Oliver, *Struct. Multidiscip. Optimiz.* **2021**, *63*, 955.
[52] Y. Han, B. Xu, Y. Liu, *Struct. Multidiscip. Optimiz.* **2021**, *63*, 2571.
[53] R. Picelli, R. Sivapuram, Y. M. Xie, *Struct. Multidiscip. Optimiz.* **2021**, *63*, 935.
[54] Z. Du, T. Cui, C. Liu, W. Zhang, Y. Guo, X. Guo, *Struct. Multidiscip. Optimiz.* **2022**, *65*, 158.
[55] D. Yu, S. Cai, T. Gao, W. Zhang, *Struct. Multidiscip. Optimiz.* **2023**, *66*, 10.
[56] Z. Zhuang, Y. M. Xie, Q. Li, S. Zhou, *Struct. Multidiscip. Optimiz.* **2023**, *66*, 11.
[57] Y. Zhao, G. Guo, W. Zuo, *Struct. Multidiscip. Optimiz.* **2023**, *66*, 146.
[58] G. Dong, Y. Tang, Y. F. Zhao, *J. Eng. Mater. Technol.* **2019**, *141*, 011005.
[59] M. Ozdemir, U. Simsek, E. Kuser, C. E. Gayir, A. Celik, P. Sendur, *Adv. Eng. Mater.* **2023**, *25*, 2201811.
[60] O. Parlayan, M. Ozdemir, C. E. Gayir, U. Simsek, G. Kiziltas, *Int. J. Adv. Manuf. Technol.* **2023**, *129*, 3197.
[61] M. Modrek, A. Viswanath, K. A. Khan, M. I. H. Ali, R. K. Abu Al-Rub, *Case Stud. Therm. Eng.* **2022**, *36*, 102161.
[62] L. Tian, B. Sun, X. Yan, A. Sharf, C. Tu, L. Lu, *Addit. Manuf.* **2024**, *84*, 104105.
[63] T. Silva, J. Y. Lu, R. K. Abu Al-Rub, D. W. Lee, *Int. J. Mech. Mater. Des.* **2024**, *20*, 317.
[64] U. Simsek, A. Akbulut, C. E. Gayir, C. Basaran, P. Sendur, *Int. J. Adv. Manuf. Technol.* **2021**, *115*, 657.
[65] D. Li, L. Wenhe, D. Ning, M. X. Yi, *Materials* **2019**, *12*, 2183.
[66] S. Xu, J. Shen, S. Zhou, X. Huang, Y. M. Xie, *Mater. Des.* **2016**, *93*, 443.
[67] D. Petraroia, https://www.mathworks.com/MATLABcentral/fileexchange/67320-stiffness-matrix-for-8-node-hexahedron, MATLAB Central File Exchange. (accessed: January 2024).
[68] W. E. Lorensen, H. E. Cline, *SIGGRAPH Comput. Graphics* **1987**, *21*, 163.
[69] U. Simsek, M. Ozdemir, P. Sendur, *Mater. Des.* **2021**, *210*, 110039.
[70] O. Gülcan, K. Günaydın, A. Tamer, *Polymers* **2021**, *13*, 2829.
[71] O. Gülcan, K. Günaydın, A. Çelik, *Aerospace* **2022**, *9*, 82.